


## Flexible method for generating needle-shaped beams and its application in optical coherence tomography: supplement

JINGJING ZHAO,<sup>1</sup> YONATAN WINETRAUB,<sup>1,2,3,4</sup> LIN DU,<sup>5</sup>  AIDAN VAN VLECK,<sup>1</sup> KENZO ICHIMURA,<sup>6,7,8</sup> CHENG HUANG,<sup>9</sup> SUMAIRA Z. AASI,<sup>10</sup> KAVITA Y. SARIN,<sup>10</sup> AND ADAM DE LA ZERDA<sup>1,2,3,4,11,\*</sup>

<sup>1</sup>*Department of Structural Biology, Stanford University School of Medicine, Stanford, California 94305, USA*

<sup>2</sup>*Biophysics Program at Stanford, Stanford, California 94305, USA*

<sup>3</sup>*Molecular Imaging Program at Stanford, Stanford, California 94305, USA*

<sup>4</sup>*The Bio-X Program, Stanford, California 94305, USA*

<sup>5</sup>*Department of Electrical and Systems Engineering, University of Pennsylvania, Philadelphia, Pennsylvania 19104, USA*

<sup>6</sup>*Division of Pulmonary, Allergy and Critical Care, Stanford University School of Medicine, Stanford, California 94305, USA*

<sup>7</sup>*Vera Moulton Wall Center of Pulmonary Vascular Disease, Stanford University School of Medicine, Stanford, California 94304, USA*

<sup>8</sup>*Cardiovascular Institute, Stanford University School of Medicine, Stanford, California 94304, USA*

<sup>9</sup>*Department of Biology, Stanford University, Stanford, California 94305, USA*

<sup>10</sup>*Department of Dermatology, Stanford University School of Medicine, Stanford, California 94305, USA*

<sup>11</sup>*The Chan Zuckerberg Biohub, San Francisco, California 94158, USA*

\*Corresponding author: [adlz@stanford.edu](mailto:adlz@stanford.edu)

---

This supplement published with Optica Publishing Group on 22 July 2022 by The Authors under the terms of the [Creative Commons Attribution 4.0 License](https://creativecommons.org/licenses/by/4.0/) in the format provided by the authors and unedited. Further distribution of this work must maintain attribution to the author(s) and the published article's title, journal citation, and DOI.

Supplement DOI: <https://doi.org/10.6084/m9.figshare.20145608>

Parent Article DOI: <https://doi.org/10.1364/OPTICA.456894>

1 **Flexible method for generating needle-**  
2 **shaped beams and its application in optical**  
3 **coherence tomography**

4 **JINGJING ZHAO<sup>1</sup>, YONATAN WINETRAUB<sup>1,2,3,4</sup>, LIN DU<sup>6</sup>, AIDAN VAN VLECK<sup>1</sup>,**  
5 **KENZO ICHIMURA<sup>7,8,9</sup>, CHENG HUANG<sup>10</sup>, SUMAIRA Z. AASI<sup>11</sup>, KAVITA Y.**  
6 **SARIN<sup>11</sup>, ADAM DE LA ZERDA<sup>1,2,3,4,5,\*</sup>**

7 *<sup>1</sup>Department of Structural Biology, Stanford University School of Medicine, Stanford, California,*  
8 *94305, USA*

9 *<sup>2</sup>Biophysics Program at Stanford, Stanford, California, 94305, USA*

10 *<sup>3</sup>Molecular Imaging Program at Stanford, Stanford, California, 94305, USA*

11 *<sup>4</sup>The Bio-X Program, Stanford, California, 94305, USA*

12 *<sup>5</sup>The Chan Zuckerberg Biohub, San Francisco, California, 94158, USA*

13 *<sup>6</sup>Department of Electrical and Systems Engineering, University of Pennsylvania, Philadelphia,*  
14 *Pennsylvania, 19104, USA*

15 *<sup>7</sup>Division of Pulmonary, Allergy and Critical Care, Stanford University School of Medicine, Stanford,*  
16 *California, 94305, USA*

17 *<sup>8</sup>Vera Moulton Wall Center of Pulmonary Vascular Disease, Stanford University School of Medicine,*  
18 *Stanford, California, 94304, USA*

19 *<sup>9</sup>Cardiovascular Institute, Stanford University School of Medicine, Stanford, California, 94304, USA*

20 *<sup>10</sup>Department of Biology, Stanford University, Stanford, California, 94305, USA*

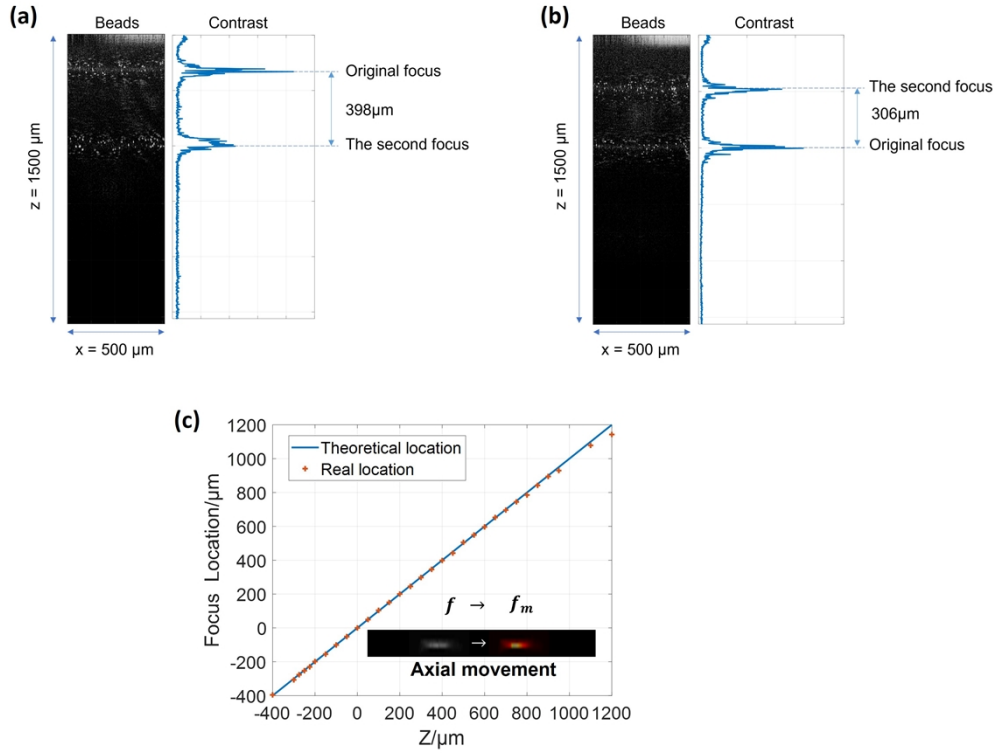
21 *<sup>11</sup>Department of Dermatology, Stanford University School of Medicine, Stanford, California 94305,*  
22 *USA*

23 *\* [adlz@stanford.edu](mailto:adlz@stanford.edu)*

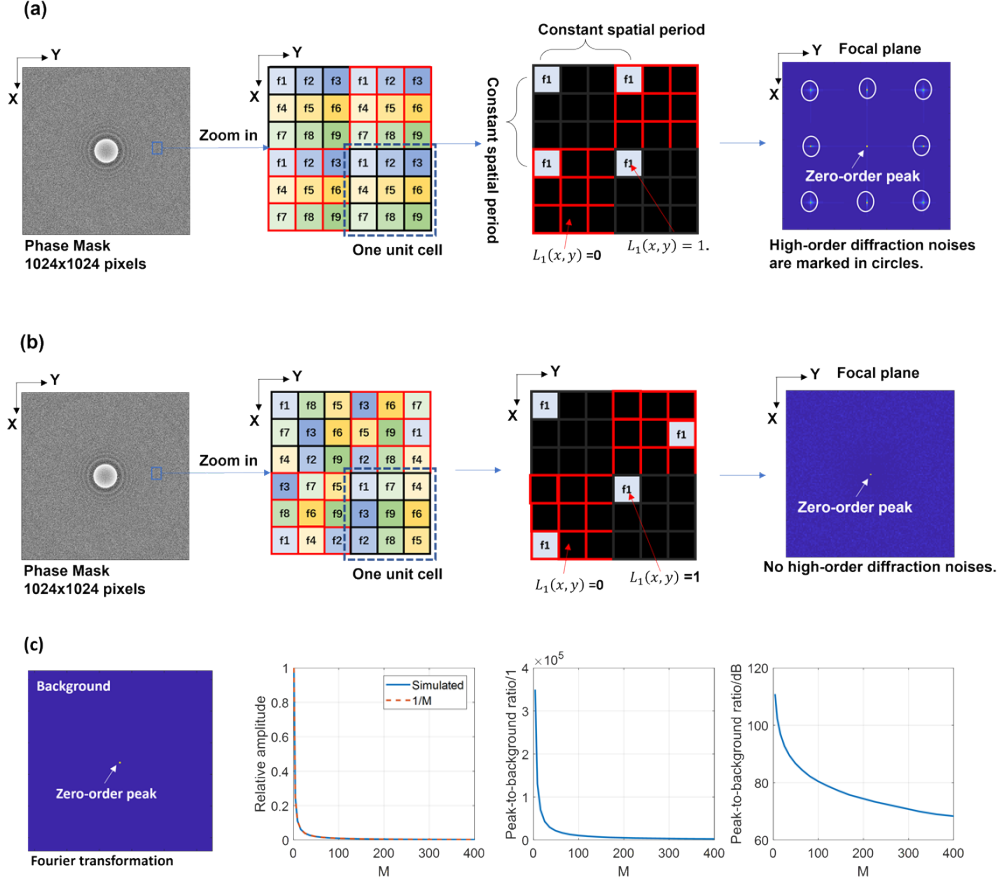
24 **1. Introduction**

25 **2. Methods**

26 **2.1 Principle**

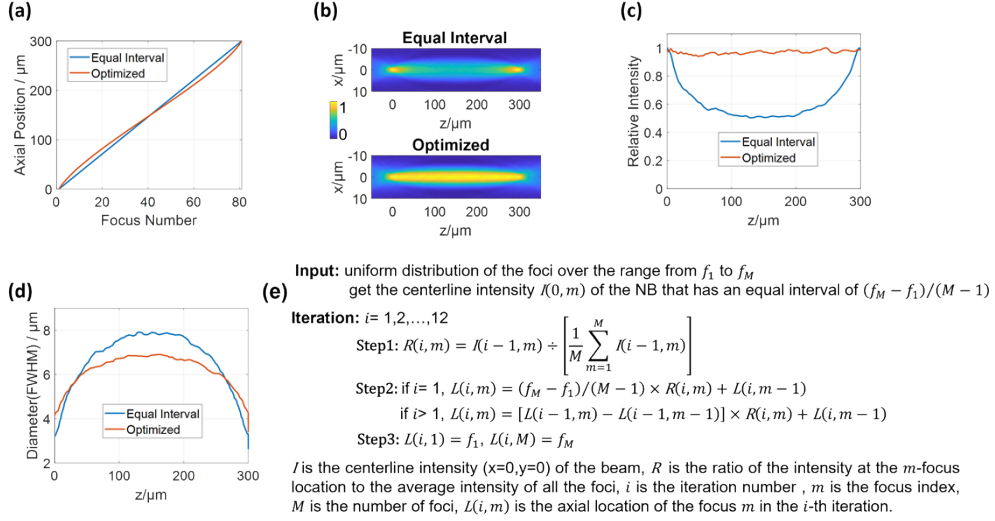


27 **Fig.S1** The experimental demonstration of the focus shift function. The DOEs containing two foci were fabricated and placed in OCT system (referring to **Fig.S10**). One focus is the  
28 original objective focus  $f$ , and the other is shifted to  $f_m$  according to the function  $P_m$   
29  $(x,y,f_m,f) = (2\pi n/\lambda) \cdot \left\{ \left[ f - \sqrt{f^2 - (x^2 + y^2)} \right] - \left[ f_m - \sqrt{f_m^2 - (x^2 + y^2)} \right] \right\}$ , where  $(x,y)$   
30 is the planar coordinate,  $\lambda$  is the light wavelength, and  $n$  is the diffractive index of the  
31 imaging space. (a, b) OCT B-scan images ( $x$  is the horizontal direction and  $z$  is the depth  
32 direction) of the  $0.8\mu\text{m}$  beads. In a B-scan, there are two separate bright layers due to the two  
33 foci. The two focal planes were determined by the two intensity peaks and the interval  
34 between the two peaks was measured to compare the designed shift  $(f_m - f)$ . The shifts in  
35 the figures are  $400\mu\text{m}$  and  $-300\mu\text{m}$ . (c) The experimental results are consistent with the  
36 theoretical values in the range of  $[-400\mu\text{m}, 1200\mu\text{m}]$  with the errors between 1% and 5%, and  
37  $z = 0$  is the original focal location.  
38  
39



40  
41  
42  
43  
44  
45  
46  
47  
48  
49  
50  
51  
52  
53  
54  
55  
56  
57  
58  
59  
60

**Fig.S2** The method to allocate the pixels of the phase mask to different foci. This example contains 9 foci and  $1024 \times 1024$  pixels. (a) Every  $3 \times 3$  contiguous pixels make up one unit cell (four unit cells in the zoom-in view). The 9 pixels in one unit cell are assigned to the 9 foci, for example, the pixel labeled with  $f_1$  means  $L_1(x,y) = 1$  and  $L_{m \neq 1}(x,y) = 0$  ( $m \in \{1,2,\dots,9\}$ ). The locations of the pixels associated with the same focus in different unit cells are constant. For example, all the four  $f_1$  pixels are located in the top left corner of four  $3 \times 3$  unit cells, and  $L_1(x,y) = 1$  is periodic in both  $X$  and  $Y$  directions. In this manner, each binary function  $L_m(x,y)$  is a two-dimensional periodic array. The periodic distributions introduce 8 apparent high-order peaks in the focal plane, generating 9 beams in total. (b) In order to eliminate noisy high-order beams, the locations of the pixels assigned to a specific focus are random in different unit cells. Since the spatially periodic property of  $L_m(x,y)$  is broken, only the zero-order beam at the center of the focal plane remains. The intensity ratio of the central beam to the background is 102dB in the simulations. In real applications, the number of foci can be huge, for example, 400 foci. (c) The amplitude of the zero-order peak is inversely proportional to the foci number  $M$ . The background noise level also decreases with  $M$ . Overall, the peak-to-background ratio (PBR) decreases with  $M$ , but PBR keeps a large value even at  $M=400$  (PBR>3100). Here, PBR is calculated as the ratio of peak intensity to the average background intensity.



61

62 **Fig.S3** The positions of the individual foci are optimized for the uniform axial intensity of the  
 63 generated beam. In this simulation example, the beam is composed of 81 foci with the length  
 64 of  $300\mu\text{m}$ , and the lens is a 20x water immersion objective (UMPLFLN20XW, Olympus,  
 65 equivalent focal length = 9mm). (a) Two spatial distributions of the foci. In one, the foci are  
 66 uniformly distributed over the range  $0\text{-}300\mu\text{m}$  with an equal interval (the objective original  
 67 focus is at  $z = 0$ ), while in the second the foci locations are optimized by the algorithm listed  
 68 in e. (b) If the foci are uniformly distributed, the axial beam intensity is not uniform, which  
 69 creates maximums at the two ends of the beam. With optimized foci positions, the beam  
 70 displays uniform intensity distribution along the  $z$  direction. (c) A comparison of axial beam  
 71 intensities under the two conditions. With optimization, the intensity fluctuation is reduced  
 72 from 50% to 5%. (d) Optimization is also beneficial to narrow the maximum diameter of the  
 73 needle-shaped beam. (e) The algorithm developed in this study to uniform the beam axial  
 74 intensity by optimizing the foci positions. To accelerate the optimization of foci positions, we  
 75 only calculate the light distribution along the optical axis ( $x = 0$  and  $y = 0$ ,  $z$  has 1024 pixels)  
 76 and the number of iterations is fixed at 12. The computation time cost for 100 foci is 1.6s (I7-  
 77 8700 3.2GHz, 64Gb RAM) or 1.4s (AMD 3945WX 4.0GHz, 160Gb RAM). For 400 foci, it is  
 78 5.5s (I7-8700 3.2GHz, 64Gb RAM) or 5.0s for 400 foci (AMD 3945WX 4.0GHz, 160Gb  
 79 RAM).

80

81 **2.2 Simulations**

82 Phase adjuster affects several characteristics of NB. Here we selected several simulation  
 83 experiments to reveal its role on shaping the NB profile. We use phase adjusters  $Pa_m = PA \cdot$   
 84  $m$ , where the focus index  $m$  and  $PA$  is the coefficient.

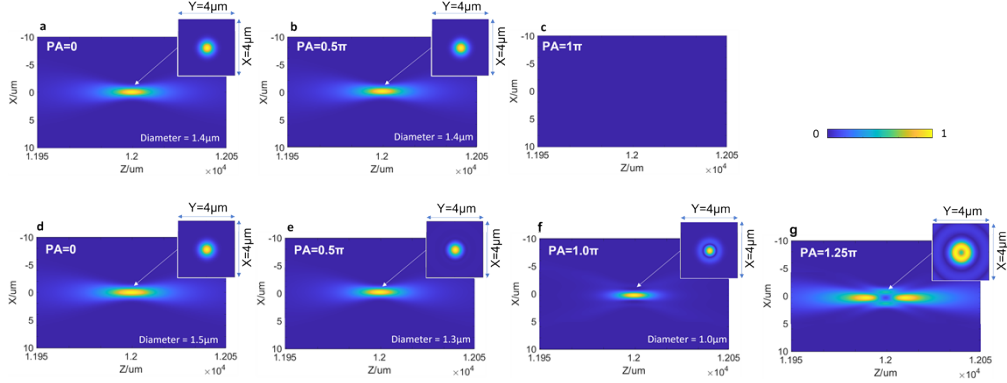
85 The first example is a two-foci beam. The focus is  $F(x,y,z,f) = A(x,y,z,f) \exp$   
 86  $[i \cdot P(x,y,z,f)]$ , where  $A$  is the amplitude and  $P$  denotes phase distribution, referring to Eq.  
 87 (3) and Eq. (4) in the main text. Set the axial interval between the two foci as zero and the  
 88 phase adjuster is zero, then the two foci are the same as  $F(x,y,z,f)/2$ , generating a single  
 89 bright focus  $F(x,y,z,f)$  with a FWHM diameter of  $1.4\mu\text{m}$ , as shown in **Fig.S4(a)**. Adding a  
 90 phase shift  $\pi/2$  to the second focus, the combination is  $F(x,y,z,f) \cdot 0.5 \cdot [1 + \exp(i \cdot \pi/2)]$ ,  
 91 and the amplitude is reduced to  $A/\sqrt{2}$  and the diameter is unchanged, as shown in **Fig.S4(b)**.  
 92 With the phase shift of  $\pi$ , the two foci counteract each other, as shown in **Fig.S4(c)**. It proves  
 93 that the combined optical field can be modulated by adjusting the phase difference between  
 94 the two spatially coincident foci.

95 Second, set the axial interval between the two foci as  $4\mu\text{m}$ . If the phase shift is zero,  
 96 **Fig.S4(d)**, the two foci have the same phase distribution along the optical axis, the light filed  
 97 is  $[F(x,y,z,f - 2\mu\text{m}) + F(x,y,z,f + 2\mu\text{m})]/2$ , and the diameter at the middle plane between  
 98 the two foci is  $1.5\mu\text{m}$  (larger than the single-focus diameter  $1.4\mu\text{m}$ ), given by  
 99  $[F(x,y,f,f - 2\mu\text{m}) + F(x,y,f,f + 2\mu\text{m})]/2$ . With a non-zero  $PA$ , the light filed is  
 100  $[F(x,y,z,f - 2\mu\text{m}) + F(x,y,z,f + 2\mu\text{m}) \cdot \exp(i \cdot PA)]/2$ . By increasing the  $PA$  in **Fig.S4(e-**  
 101 **g)**, the optical field created by the interference of the two foci changes in terms of intensity,  
 102 diameter, and side lobes. With increasing  $PA$ , the diameter can reduce to be smaller than the  
 103 original objective focal size at the cost of the intensity, as shown in **Fig.S4(e, f)**. With a larger  
 104 value of  $PA$ , donut focus may be generated, **Fig.S4(g)**.

105 Third, we tested three closely-spaced foci with a  $4\mu\text{m}$  interval. As illustrated in **Fig.S5(a-**  
 106 **e)**, a large value of  $PA$  can reduce beam diameter (even smaller than the Gaussian beam  
 107 focus) and the length of the three-foci beam. At a distant position, e.g.,  $z=12.025\text{mm}$  in  
 108 **Fig.S5(d-e)**, the intensity of the three-foci beam with a large  $PA$  is much weaker than that of  
 109 the one modulated by a small  $PA$ . In other words, more energy will leak into the neighboring  
 110 space when using a small  $PA$ . For a NB containing many foci, like the NBs in **Fig.S10**, with a  
 111 large  $PA$ , NB has a small diameter and the beam profile at a certain depth  $Z'$  is mainly  
 112 determined by the few local foci around  $Z'$  (barely affected by the distant foci), thus the NB  
 113 diameter is more uniform along  $z$  direction. On the contrary, a small  $PA$  leads to a large NB  
 114 diameter and makes it hard for the current optimization algorithm (**Fig.S3**) to simultaneously  
 115 achieve uniform axial intensity and uniform beam diameter along the depth direction. As  
 116 mentioned in Discussion section of the main text, both uniform intensity and uniform  
 117 diameter are promisingly achievable if we can develop a new design algorithm that fully  
 118 leverages the design freedom of  $f_1, \dots, f_M$  and  $Pa_1, \dots, Pa_M$ .

119 Next, based on the above simulated results, it is reasonable to surmise that a NB  
 120 composed of multiple foci can also be modulated by the phase adjuster in a similar way,  
 121 which has been testified in **Fig.2**. Conclusively, a large  $PA$  reduces the diameter at the cost of  
 122 side lobes and efficiency.

123



124

125

126

127

128

129

130

131

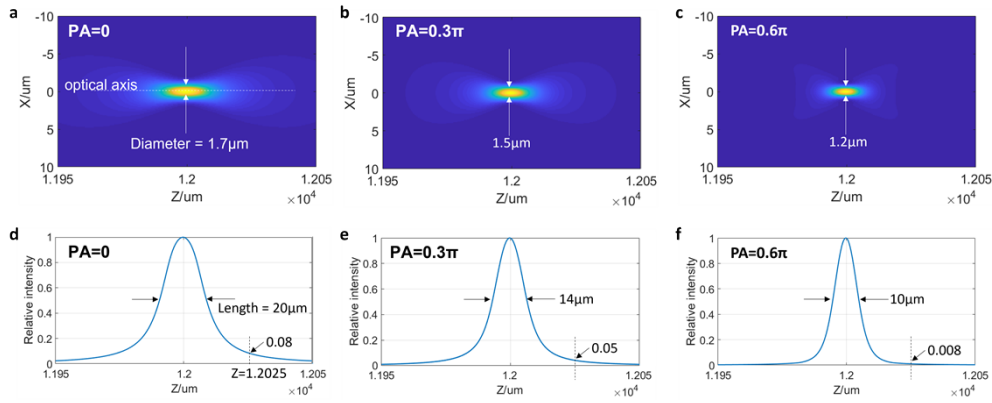
132

133

134

135

**Fig.S4** Simulations of two foci. The incident light is Gaussian beam (910nm, 4.6mm diameter at  $1/e^2$ , intensity = 1), focused by a water immersion objective (focal length in water = 12mm). The two foci are spatially coincident in (a-c). (a)  $PA=0$ , beam diameter =  $1.4\mu\text{m}$ , maximum intensity =  $4 \times 10^6$ ; (b)  $PA=0.5\pi$ , beam diameter =  $1.4\mu\text{m}$ , intensity =  $2 \times 10^6$ ; (c)  $PA=1\pi$ , intensity = 0. The two foci are separately fixed at  $Z=12\text{mm}-2\mu\text{m}$  and  $Z=12\text{mm}+2\mu\text{m}$  in (d-g). (d)  $PA=0$ , beam diameter =  $1.5\mu\text{m}$ , intensity =  $3.3 \times 10^6$ , invisible side lobes; (e)  $PA=0.5\pi$ , beam diameter =  $1.3\mu\text{m}$ , intensity =  $2.9 \times 10^6$ , invisible side lobes; (f)  $PA=1\pi$ , beam diameter =  $1.0\mu\text{m}$ , intensity =  $0.4 \times 10^6$ , intensity ratio of the side lobe to the central main lobe is 4%; (g)  $PA=1.25\pi$ , intensity =  $1.4 \times 10^5$ , donut spot.



136

137

138

139

140

141

142

143

144

145

146

**Fig. S5** Simulations of a 3-foci beam. The incident light is Gaussian beam (910nm, 4.6mm diameter at  $1/e^2$ , intensity = 1), focused by a 20x water immersion objective (focal length = 12mm). The Z positions of the three foci are 12mm-4μm, 12mm, 12mm+4μm. (a)  $PA=0$ , beam diameter =  $1.7\mu\text{m}$ , maximum intensity =  $2.5 \times 10^6$ ; (b)  $PA=0.3\pi$ , beam diameter =  $1.5\mu\text{m}$ , intensity =  $2.7 \times 10^6$ ; (c)  $PA=0.6\pi$ , beam diameter =  $1.2\mu\text{m}$  (Gaussian beam focus size is  $1.4\mu\text{m}$ ), intensity =  $0.9 \times 10^6$ . (d-f) With increasing  $PA$ , the length of the beam, described by FWHM of the axial intensity along the optical axis, becomes shorter ( $20\mu\text{m}$ ,  $14\mu\text{m}$ , and  $10\mu\text{m}$ ), and more energy is confined around the physical positions of the three foci.

- Step 1
- Choose the beam length  $L$  and determine the number of the foci  $M$  with the restriction of  $RL \leq L/(M - 1) \leq RL$ , where  $RL$  stands for Rayleigh length of the objective.
  - Select the position of the first focus, which is usually set at  $f_1 = f$  or  $f_1 = f - L/2$ , where  $f$  is the objective focal length, then the last focus location is  $f_M = f_1 + L$ . We used  $f_1 = f$  for all the DOEs fabricated in this study.
- Step 2
- Optimize the positions of the individual foci for the uniform axial intensity of the generated beam, as illustrated in Fig. S3.
- Step 3
- The phase adjusters  $Pa_1, \dots, Pa_M$  are set at  $Pa_m = PA \cdot m$  in this work, where  $m$  is the focus index  $\in \{1, 2, \dots, M\}$  and  $PA$  is a coefficient  $\in [0, 2\pi]$ .
  - Scan  $PA$  within the range of  $[0, 2\pi]$ , thereby quantifying the beam characteristics under different  $PA$  values. Empirically,  $0 < PA < 0.5\pi$  is the common range for NBs.
- Step 4
- Select an appropriate  $PA$  for a design.
  - Complete the phase pattern of the designed needle beam, as described in Fig. 1.

147

148 **Fig.S6** The design procedure of a needle-shaped beam.

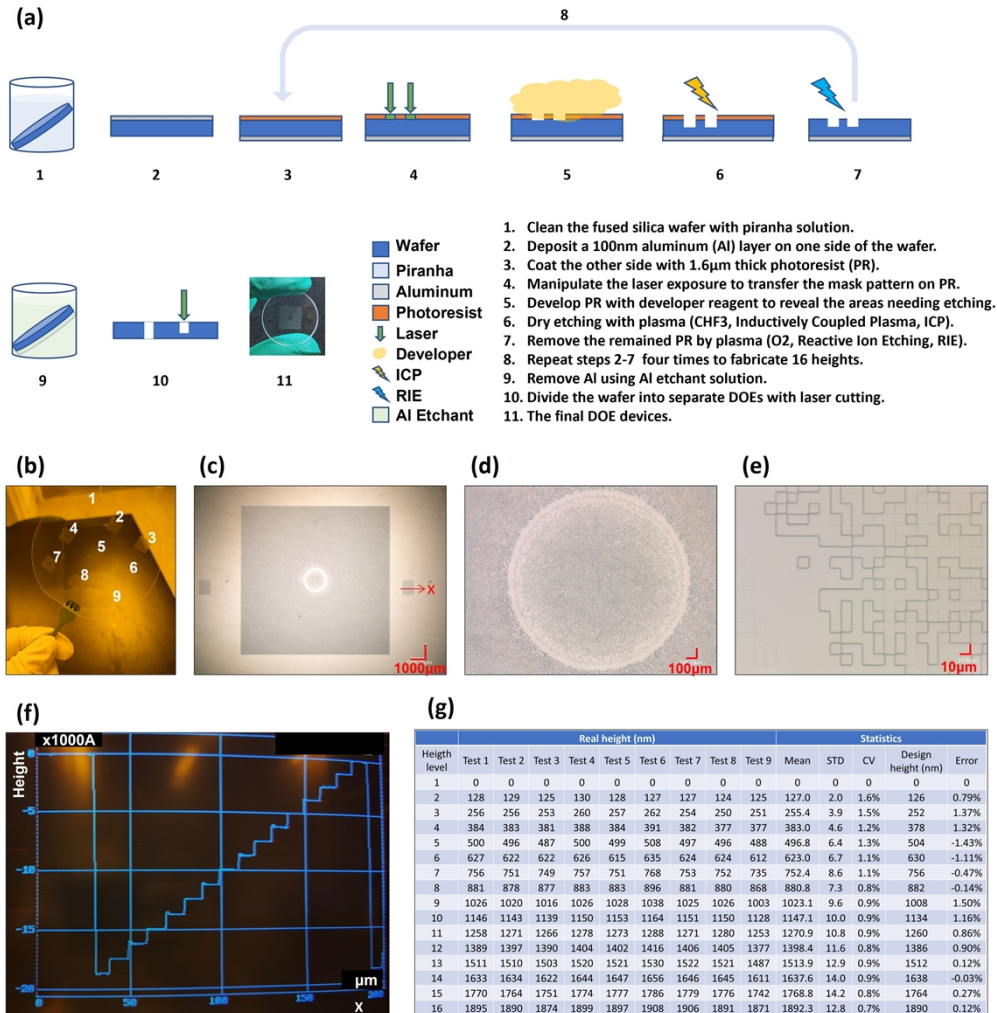
149

### 150 2.3 Fabrication

151 The fabrication procedure is shown in **Fig.S7**. A blank fused silica wafer (4inch, 500 $\mu$ m  
 152 thickness) was first soaked in piranha solution (9:1 H<sub>2</sub>SO<sub>4</sub>:H<sub>2</sub>O<sub>2</sub>) for 20mins at 120°C for  
 153 cleaning. Then a 100nm thick aluminum (Al) layer was deposited onto one side of the wafer  
 154 (750 seconds, Lesker Sputter). The Al layer serves as a heat conductor to improve the  
 155 downstream dry etching uniformity. With the coating tool (SVG Coat), a 1.6 $\mu$ m thick  
 156 photoresist (SPR3612, 2mm edge bead removal) was deposited onto the other side of the  
 157 wafer after being processed by Hexamethyldisilazane (HDMS, an adhesion promoter for  
 158 resists). The mask pattern was transferred onto the photoresist layer by direct laser writing  
 159 (MLA 150, Heidelberg; 405nm laser, 1 defocus, 50mJ/cm<sup>2</sup> dosage). Next, the wafer was  
 160 baked at 110°C for 90s to harden the exposed photoresist then developed (SVG Developer).  
 161 Then, the wafer was engraved by inductively coupled plasma (ICP) etching (ICP Dielectric  
 162 Etcher, Plasma Therm Versaline; the parameters were set as 450W ICP, 50W BP, 40CHF<sub>3</sub>, 2  
 163 O<sub>2</sub>, 5 mT, 4T He, 10°C electrode, 70°C liner, 90°C spool, 90°C lip). The etching rate was  
 164 2.3-2.5nm/s, measured using a dummy wafer. Following etching, the remaining photoresist  
 165 was removed by oxygen plasma (Plasma Resist Strip, Matrix). The lithography steps  
 166 described above were repeated three more times (the first round lithography for 1008nm, the  
 167 second for 504nm, the third for 252nm, and the fourth for 126nm, combining to generate 16  
 168 heights). The Al layer was removed by first soaking the wafer in aluminum etchant (CMOS,  
 169 J.T. Baker) at 40°C for 20mins, and then cleansing in piranha solution (20mins at 120°C).  
 170 Finally, wafers were divided into separate DOEs using an Excimer laser (IX-255, IPG  
 171 Photonics; 193nm, under high fluence mode, 7mJ, VAT=35%, 4 repeated cycles).

172





173

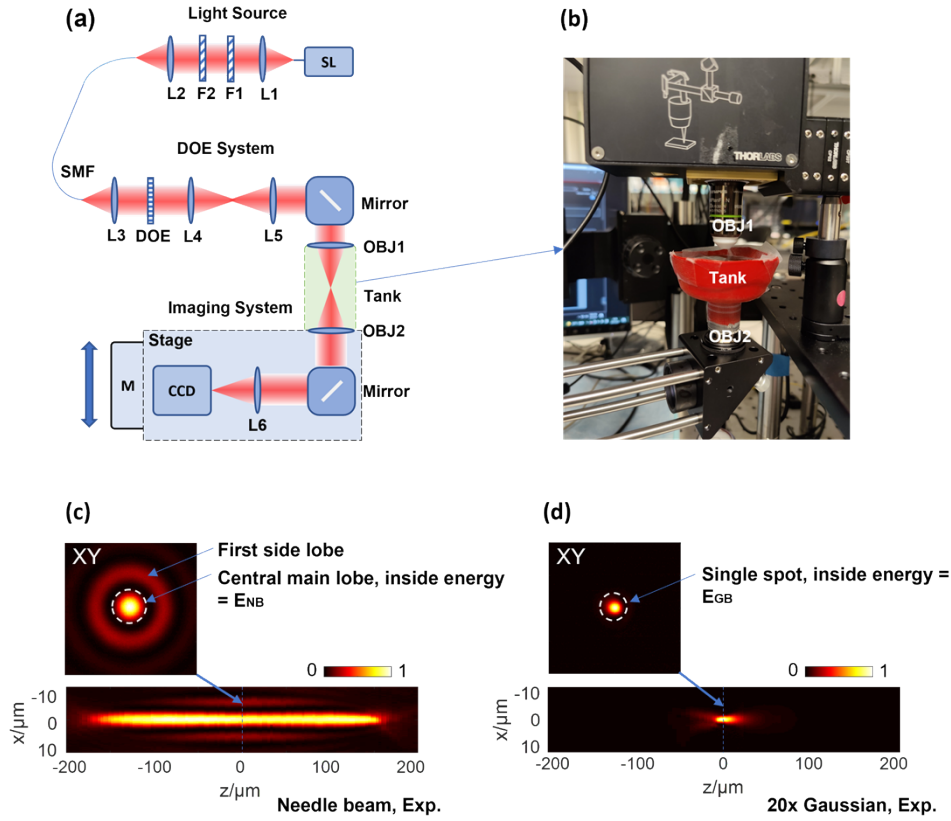
174 Fig.S7 The fabrication of the DOEs. (a) The fabrication process for the DOEs is based on  
 175 four rounds of lithography. (b) Nine DOEs were fabricated on one wafer simultaneously. (c)  
 176 The full-view microphotograph of one DOE (VHX-6000, Keyence). (d) A zoomed-in view of  
 177 the DOE. (e) A close-up view of the individual 10 $\mu\text{m}$  × 10 $\mu\text{m}$  pixels on the DOE surface. (f)  
 178 The 16 height levels of a step structure (the red arrow in c) are measured by the profilometer  
 179 (P2, Tencor). (g) The real 16 heights of 9 samples are tested and the errors are below 2%.  
 180 STD stands for standard deviation, and CV is coefficient of variation.

181

182 **3. Results**

183 **3.1 Beam profiles**

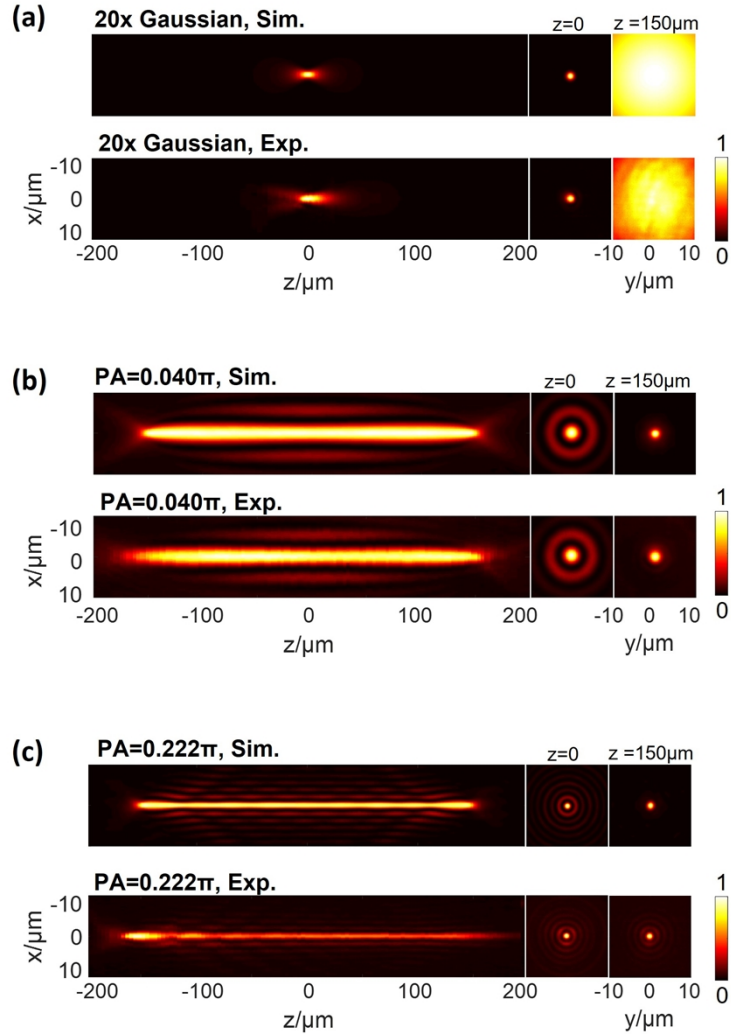
184 Beam profiles were measured by a microscope system shown in **Fig.S8**. Its magnification is  
185 44.4 when using 40x water immersion objective (UMPLFLN40XW, Olympus) for imaging  
186 and is 11.1 with a 10x dry lens (LSM02-BB, Thorlabs). The axial scanning step size was  
187 chosen between 1 $\mu$ m to 10 $\mu$ m to match different beam lengths. The beam diameter (FWHM)  
188 in a 2D image is calculated as  $2 \times \sqrt{A_{FWHM}/\pi}$ , where  $A_{FWHM}$  is the area where the beam  
189 intensity is no less than the half of the maximum intensity (after background subtraction). As  
190 show in **Fig.S8(c)**, the cross section through the middle of the NB or focused Gaussian beam  
191 is taken out to calculate the efficiency and sidelobe ratio. The sidelobe ratio is the peak  
192 intensity ratio between the first sidelobe and the main lobe, and the needle-shaped beam (NB)  
193 efficiency is evaluated by the ratio of the energy enclosed within the NB's central lobe to the  
194 energy enclosed within the Gaussian focus spot. When calculating the efficiency, the focused  
195 Gaussian beam is generated by the same objective used for NBs. In theory, the efficiency of  
196 Gaussian beam is 100% since its focus contains all the incident energy ( $E_{IN}$ ),  $E_{GB} = E_{IN}$ . In the  
197 simulations, the input energy (the energy of the Gaussian beam before entering the objective)  
198 is the same as the energy enclosed within the Gaussian focal spot, generating a 100%  
199 efficiency. In the practical experiments of 3D beam profiles, the transmission efficiency of  
200 the objective ( $EE_{OBJ}$ ) is not 100%. Thus, the Gaussian spot energy is lower than the incident  
201 energy. The energy of the Gaussian spot is  $E_{GB} = EE_{OBJ} \times \text{Input Energy}$ . The energy of the  
202 main lobe of the NB is  $E_{NB} = EE_{OBJ} \times \text{Input Energy} \times E_{NB}$ . So we use the energy of the  
203 Gaussian focus as the reference to eliminate the effect of objective on energy transmission,  
204 giving  $E_{NB}/E_{GB} = (EE_{OBJ} \times \text{Input Energy} \times E_{NB}) / (EE_{OBJ} \times \text{Input Energy}) = EE_{NB}$ .  
205



206

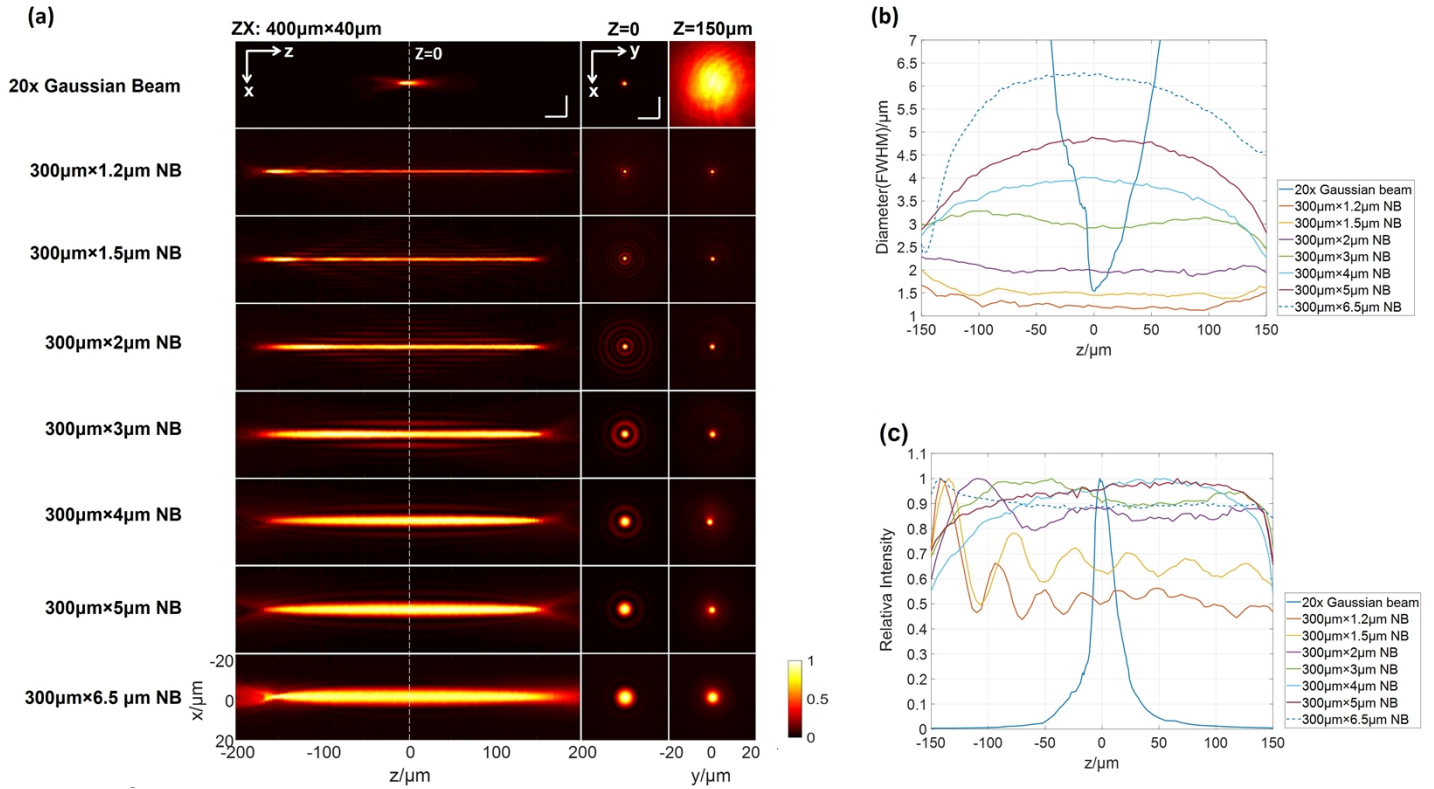
207 **Fig.S8** The setup used to image the beam profiles. (a) This setup contains the three modules  
 208 of light source, the DOE system, and the imaging system. The light is produced by a  
 209 supercontinuum laser (SL, Superk Extreme, NKT Photonics). Lens L1 collimates the output  
 210 light from the single mode fiber (SMF). F1 is a bandpass filter ( $910\pm 5\text{nm}$ , FB910-10,  
 211 Thorlabs) and F2 is a neutral density filter to reduce the power. L2 is the coupler (focal length  
 212 = 12mm, TC12APC-850, Thorlabs) to convey the laser into the downstream SMF. L3 is the  
 213 collimator with a focal length of 25mm and the output Gaussian beam has a diameter of  
 214 4.6mm. The homemade DOE aims to modulate the beam phase. The pair of L4 and L5 (focal  
 215 length = 60mm, AC254-060-B, Thorlabs) is a 4f system to transfer the phase pattern to the  
 216 back focal plane of the 20x water immersion objective OBJ1 (UMPLFLN20XW, Olympus).  
 217 The beam is focused by OBJ1 in the water of the tank and observed by another 40x water  
 218 immersion objective OBJ2 (UMPLFLN40XW, Olympus) with the lens L6 (focal  
 219 length=200mm, AC254-200-B, Thorlabs). The beam is imaged on the CCD sensor (pixel size  
 220 = 5  $\mu\text{m}$ , WinCamD, Dataray). The imaging system is axially moved by a precise motor M  
 221 (Z812, Torlabs) to test the beam profiles at different depths. (b) A photo of the two objectives  
 222 and tank. (c, d) The sidelobe ratio of NB is the peak intensity ratio between the first sidelobe  
 223 and the main lobe, and the NB's efficiency is the ratio of the energy enclosed within the NB's  
 224 central lobe (white circle) to the energy enclosed within the Gaussian focus spot ( $=E_{NB}/E_{GB}$ ).

225

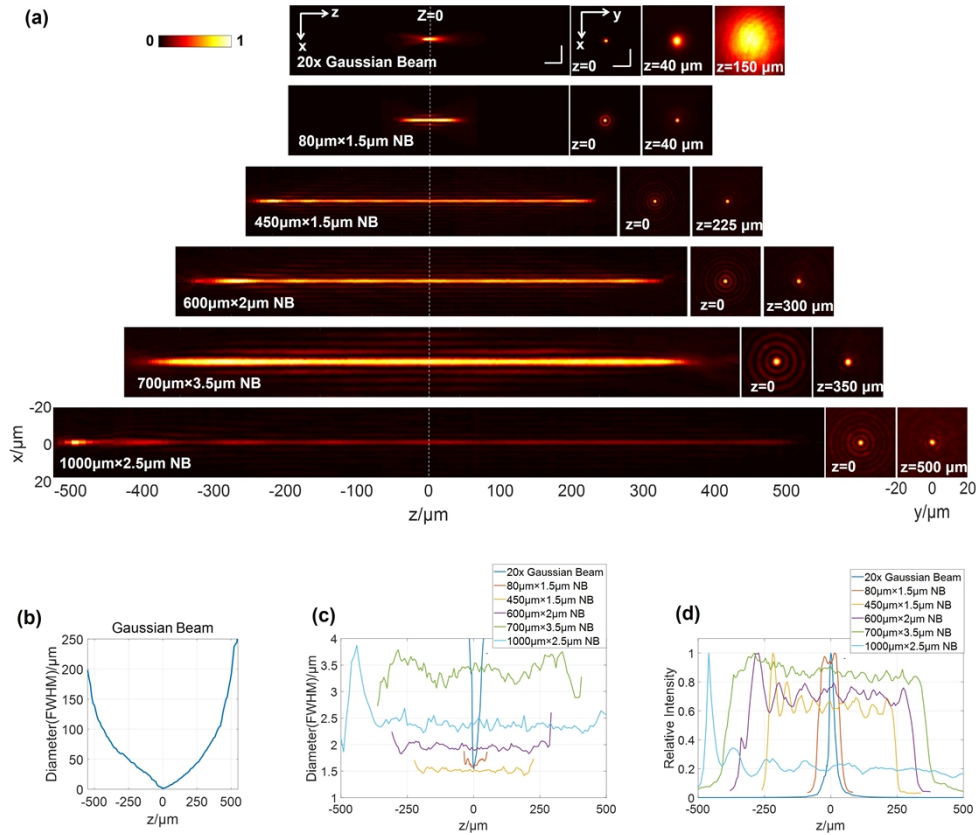


226

227 **Fig.S9** The real beam profiles versus the simulations. (a) The real profiles of the Gaussian  
 228 beam (910nm, 4.6mm diameter at  $1/e^2$ ), focused by 20x water immersion objective. The  
 229 experimental focal size is  $1.6\mu\text{m}$  and the simulated size is  $1.5\mu\text{m}$ . (b), The  $300\mu\text{m}$  needle-  
 230 shaped beam (NB) with the phase adjusters  $Pa_m = 0.040\pi \cdot m$  has a diameter of  $3\mu\text{m}$ .  $Pa_m$   
 231 =  $PA \cdot m$  and the focus index  $m \in \{1,2,\dots,81\}$ . (c) The  $300\mu\text{m}$  NB with  $PA = 0.222\pi$  has a  
 232  $1.2\mu\text{m}$  diameter that is smaller than the Gaussian focal spot. Sim., simulated; Exp.,  
 233 experimental.



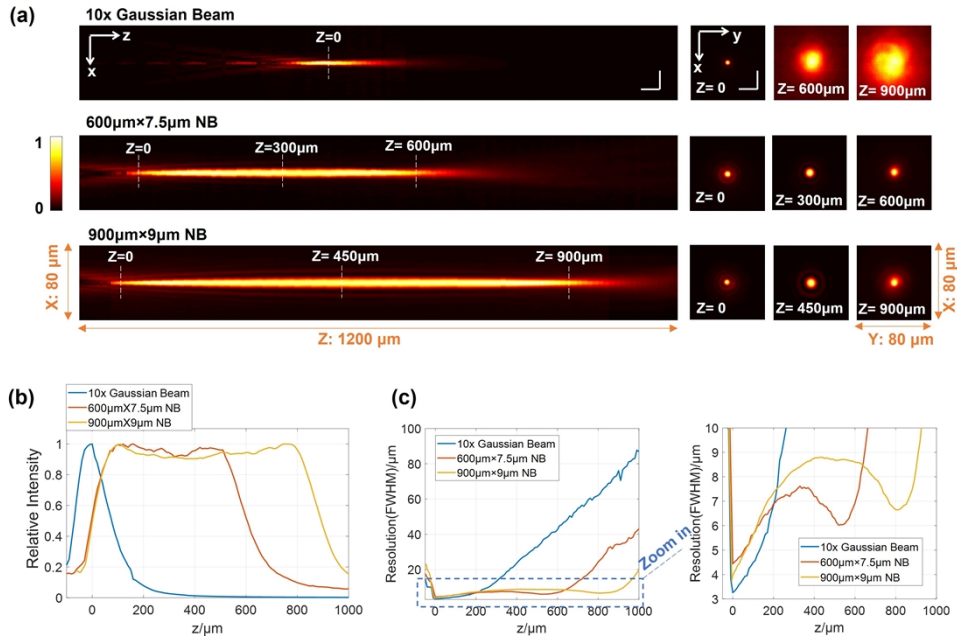
235 **Fig.S10** The real profiles of seven 300μm needle-shaped beams (NBs). (a) The real profiles.  
 236 The ZX scale bar is 25μm×10μm and the XY scale bar is 10μm×10μm. (b) The diameter  
 237 profiles. (c) The axial intensity profiles. The axial intensity of the NBs with diameters of  
 238 2μm, 3μm, 4μm, 5μm, 6.5μm is basically uniform. The narrow NB (diameter = 1.2μm or  
 239 1.5μm) has a peak at the left end because the fabrication errors lead to an intensity  
 240 increasement at the objective focus (positioned at the left end of NB), which is comparable to  
 241 the NB intensity. Gaussian beam: 910nm, 4.6mm diameter at  $1/e^2$ . The objective: 20x water  
 242 immersion objective.



243

244 **Fig.S11** The real profiles of the needle-shaped beams (NBs) with various sizes. (a) The real  
 245 profiles. The ZX scale bar is  $25\mu\text{m} \times 10\mu\text{m}$  and the XY scale bar is  $10\mu\text{m} \times 10\mu\text{m}$ . The  
 246 maximum sidelobe ratios in the middle of the NB are 20% for  $80\mu\text{m} \times 1.5\mu\text{m}$  NB, 17% for  
 247  $450\mu\text{m} \times 1.5\mu\text{m}$  NB, 18% for  $600\mu\text{m} \times 2\mu\text{m}$  NB, 11% for  $700\mu\text{m} \times 3.5\mu\text{m}$  NB, and 17% for  
 248  $1000\mu\text{m} \times 2.5\mu\text{m}$  NB. The number of the foci constituting one NB is 16 for  $80\mu\text{m} \times 1.5\mu\text{m}$  NB,  
 249 100 for  $450\mu\text{m} \times 1.5\mu\text{m}$  NB, 144 for  $600\mu\text{m} \times 2\mu\text{m}$  NB, 169 for  $700\mu\text{m} \times 3.5\mu\text{m}$  NB, and 196 for  
 250  $1000\mu\text{m} \times 2.5\mu\text{m}$  NB. The values of  $PA$  for the above NBs are  $0.210\pi$ ,  $0.190\pi$ ,  $0.104\pi$ ,  
 251  $0.035\pi$ , and  $0.129\pi$  respectively. (b) The diameter profile of the focused Gaussian beam. (c)  
 252 The diameter profiles of all beams. (d) The axial intensity distributions. Gaussian beam:  
 253  $910\text{nm}$ ,  $4.6\text{mm}$  diameter at  $1/e^2$ . The objective: 20x water immersion objective.

254

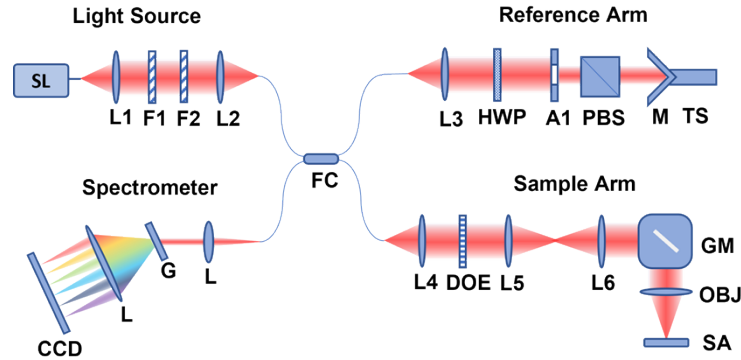


255

256 **Fig.S12** The real profiles of the needle-shaped beams (NBs) generated by non-immersion  
 257 objective. The is 10x objectives (focal length = 18mm, LSM02-BB, Thorlabs) was used as the  
 258 OBJ1 and OBJ2 in Supplementary Fig.8 with the same input Gaussian beam (910nm, 4.6mm  
 259 diameter). (a) The real profiles. The focused Gaussian beam has the Rayleigh length of 18µm  
 260 and a focal size of 3.5µm. The 600µm×7.5µm NB is contains 64 foci ( $PA = 0.096\pi$ ,  
 261 efficiency = 20%), which has a diameter profile changing between 4.5µm and 7.5µm within  
 262 its 600µm depth-of-focus (DOF). The 900µm×9µm NB has a diameter profile between 4µm  
 263 and 8.7µm within the 900µm DOF, containing 100 foci ( $PA = 0.058\pi$ , efficiency = 13%).  
 264 The maximum sidelobe ratios at the middle of NB are 5% for 600µm×7.5µm NB, 8% for  
 265 900µm×9µm NB. ZX scale bar, 35µm×20µm; XY scale bar, 20µm×20µm. (b) The axial  
 266 intensity profiles of the focused Gaussian beam and the two NBs. The uniformities of the two  
 267 NBs are both above 90%. (c) The diameter profiles. At the depth of 600µm, the focused  
 268 Gaussian beam has a diameter of 42µm, while the 600µm×7.5µm NB has a diameter of 7µm.  
 269 At the depth of 900µm, the diameter of the focused Gaussian beam is 76µm, and the diameter  
 270 of 900µm×9µm NB is only 8µm.

271

272 3.2 Needle-shaped beams in OCT  
 273  
 274



275

276 **Fig.S13** The OCT imaging system. Light source. The light is from a supercontinuum laser  
 277 (SL, Superk Extreme, NKT Photonics). Lens L1 collimates the output light from the single  
 278 mode fiber (SMF). F1 is a long-pass filter (800nm, FELH0800, Thorlabs) and F2 is a short-  
 279 pass (1050nm, #64-338, Edmund) filter. L2 is the coupler (focal length = 12mm, TC12APC-  
 280 850, Thorlabs) to convey the laser into the downstream SMF. Reference arm. L3 is the  
 281 coupler (focal length = 25mm, TC25APC-850, Thorlabs). HWP is a half-wave plate  
 282 (WPH05ME-980, Thorlabs) to reduce the polarization disparity between the reference arm  
 283 and sample arm. A1 is the adjustable aperture (SM1D12C, Thorlabs) to change the power. M  
 284 is the mirror (solid prism retroreflector, PS975M-B, Thorlabs) to reflect the input laser. PBS  
 285 is a polarizing beam-splitter cube (CCM1-PBS253/M, Thorlabs) to eliminate the reflected  
 286 light perpendicular to the input, which is induced by the mirror and can generate ghost images  
 287 in OCT. TS is a translation stage (CT1, Thorlabs) to adjust reference arm length. Sample arm.  
 288 L4 is the collimator with a focal length of 25mm and the output Gaussian beam has a  
 289 diameter of 4.6mm. The homemade DOE aims to modulate the beam phase. The pair of L5  
 290 and L6 (focal length = 60mm, AC254-060-B, Thorlabs) is a 4f system that transfers the phase  
 291 pattern to the back focal plane of the 20x water immersion objective OBJ (UMPLFLN20XW,  
 292 Olympus). GM is a two-dimensional galvo mirror (OCTP-900, Thorlabs) to scan the sample.  
 293 SA stands for sample. Spectrometer. The spectrometer is from a commercial OCT  
 294 (Ganymede OCTP-900, Thorlabs) with the detection range from 810nm to 1010nm. L, lens;  
 295 G, grating. FC is the fiber coupler (TW930R5A2, Thorlabs) to connect the above four parts.  
 296 Software. The Thorlabs Ganymede imaging software.  
 297

298 **OCT setup.** As shown in **Fig.S10**, our OCT system is based on a commercial OCT  
 299 instrument (Ganymede OCTP-900, Thorlabs) and the light source is centered at 910nm with a  
 300 bandwidth of 200nm (EXR-9 continuum laser, NKT Photonics). Its acquisition rate is 30,000  
 301 A-scans/s. The imaging depth is 2mm in air or 1.5mm in water with 1024pixels, and the  
 302 experimental axial resolution is 3 pixels (FWHM in linear scale). Its original lateral resolution  
 303 depends on the objective, which is 1.6 $\mu$ m with a 20x water immersion objective  
 304 (UMPLFLN20XW, Olympus) and 4 $\mu$ m with a 10x dry objective (LSM02-BB, Thorlabs). The  
 305 laser power entering the objective aperture is controlled below 5mW. Since our system  
 306 utilizes the same optical path (the sample arm) to illuminate the sample and collect the light  
 307 (common path), both the incident and the backscattered lights pass through the DOE (double-  
 308 passing, collected light intensity  $\propto$  the square of DOE efficiency). The OCT signal intensity  
 309 is proportional to the amplitude of the light from the sample arm (OCT intensity  $\propto$   
 310 [amplitude of sample arm signal  $\times$  amplitude of reference arm signal]). That means signal



311 intensity is linear to the square root of sample arm intensity also linearly modulated by DOE  
312 efficiency. We tested the NBs in **Fig.2** with the OCT system by scanning a metal plate in  
313 water. As listed in **Table S1**, the results prove that the signal intensity is roughly proportional  
314 to DOE efficiency. The sensitivity is measured as the ratio of metal plate intensity to the  
315 background intensity (the blank area containing no sample). The ideal point-spread function  
316 (PSF) is the same as the intensity profile of the beam. The system point-spread function  
317 (PSF)<sup>1</sup> is the product of the light illumination PSF<sub>I</sub> and the light collection PSF<sub>C</sub>. The double-  
318 passing configuration gives PSF<sub>I</sub> and PSF<sub>C</sub> the same amplitude profile of needle-shaped beam  
319 PSF<sub>NB</sub>, thus the OCT system PSF<sub>DP</sub> is the same as the intensity profile of needle-shaped beam  
320 ( $=|\text{PSF}_{\text{NB}}|^2$ ). Another possible configuration is the single-passing one, where the DOE is only  
321 used for light illumination and an independent light collection channel is required to detect  
322 the lights back-scattered from the sample. Its PSF<sub>SP</sub> is the product of PSF<sub>NB</sub> and PSF<sub>GB</sub>, where  
323 PSF<sub>GB</sub> is the 3D Gaussian amplitude profile shaped by the confocal gate of the light collection  
324 fiber via the objective. Apparently, PSF<sub>SP</sub> =  $|\text{PSF}_{\text{NB}} \times \text{PSF}_{\text{GB}}|$  makes the axial intensity  
325 reduce as well as the lateral resolution degrade with the distance to the objective focal plane.  
326 Also, double-passing configuration used in this work can suppress side lobes, since PSF<sub>DP</sub> is  
327 proportional to the intensity profile of NB while PSF<sub>SP</sub> is proportional to the amplitude profile  
328 of NB.  
329

330 **Image acquisition.** For the experiments in Figs.3-5, pixel number in both the X and Y  
331 directions was chosen as 512 (Field-of-View = 0.125mm×0.125mm, 1mm×1mm,  
332 0.5mm×0.5mm, respectively). To enhance the detection sensitivity, the A-scan at every point  
333 was repeated successively four times and the averaged data were used for image  
334 reconstruction. The acquisition time for one 3D volume is around 45s. In the reconstructed  
335 3D images, a 2D Gaussian filter with a standard deviation of 2 pixels was applied for every  
336 XY layer to reduce the speckle noises. For the dynamic imaging of drosophila larva, no A-  
337 scan average was applied in order to achieve a high frame rate (12 B-scans/s). The scanning  
338 range is 4mm in the first section of Supplementary Video and 1mm in the second and third  
339 sections, and the number of scanning steps was 2048 for all the three sections. All B-scans  
340 were processed by a 2D Gaussian filter with a standard deviation of 2 pixels to reduce speckle  
341 noise. All OCT images were presented in log10 scale. In a single 2D OCT image, the  
342 intensity scale was dynamically adjusted according to the maximum intensity and the  
343 minimum intensity (or background) in the image.  
344

345 **Beads imaging.** The phantom used to characterize the needle-shaped beams in OCT was  
346 made by uniformly distributing 0.8μm polystyrene (PS) beads (TP-08-10, Spherotech) in  
347 ultrasound gel (Aquasonic 100, Parker). The phantom was degassed with a centrifuge  
348 (15mins at 15,000rpm, ST16-R, Thermo) with bead concentration around  $2 \times 10^5/\text{mm}^3$ . The  
349 beam resolution in OCT system was tested with the 0.8μm polystyrene beads. The resolution  
350 at specific depths was determined by the average diameter (FWHM in linear scale) of bead  
351 profiles. Each XY layer containing beads in a volumetric image was measured to determine  
352 the complete resolution profile of the target beam. Within each depth, 200-300 beads were  
353 averaged to give reliable results. Additionally, 20 samples were averaged for measuring one  
354 sidelobe ratio.  
355

---

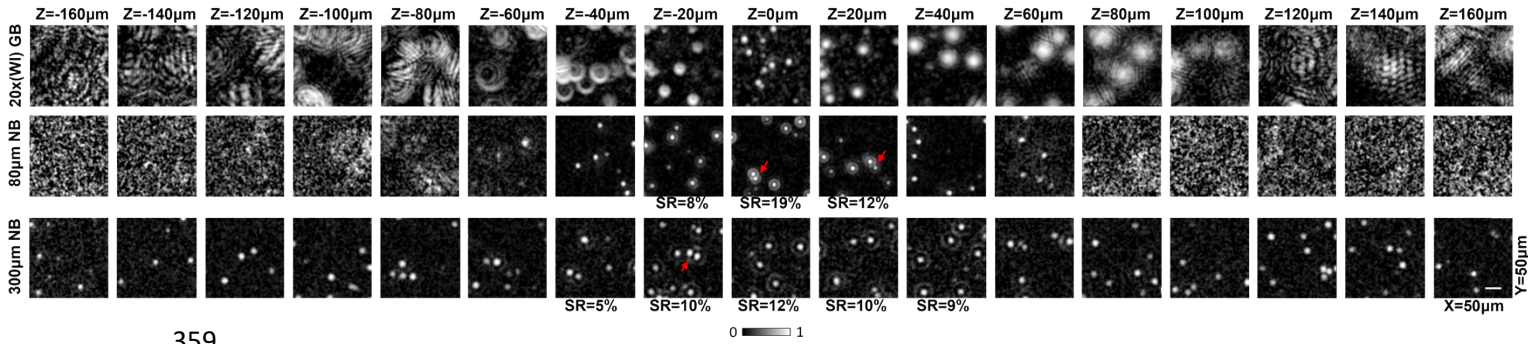
<sup>1</sup> Stelzer, E.H. and Lindek, S., 1994. Fundamental reduction of the observation volume in far-field light microscopy by detection orthogonal to the illumination axis: confocal theta microscopy. Optics Communications, 111(5-6), pp.536-547.

356 **Table R1** The quantitative characteristics of needle-shaped beams

357

<b>Beam</b>	<b>Theoretical efficiency</b>	<b>Efficiency measured by beam profiler</b>	<b>Relative intensity of metal plate in OCT</b>	<b>Intensity (I) of metal plate in OCT</b>	<b>Standard deviation (STD) of background intensity in OCT</b>	<b>Sensitivity (I/STD) measured with metal plate in OCT</b>	<b>Sensitivity measured with metal plate in OCT/dB</b>
<b>Gaussian beam</b>	100%	100.00%	100.00%	683600	180	3798	36
<b>300μm×1.2μm NB</b>	0.10%	0.30%	1.90%	12000	158	76	19
<b>300μm×1.5μm NB</b>	0.30%	0.50%	2.30%	16000	163	98	20
<b>300μm×2μm NB</b>	1%	2%	4%	26000	170	153	22
<b>300μm×3μm NB</b>	4%	4%	7%	45000	170	265	24
<b>300μm×4μm NB</b>	9%	9%	10%	70000	175	400	26
<b>300μm×5μm NB</b>	15%	22%	23%	160000	172	930	30
<b>300μm×7μm NB</b>	13%	20%	14%	95000	177	537	27

358

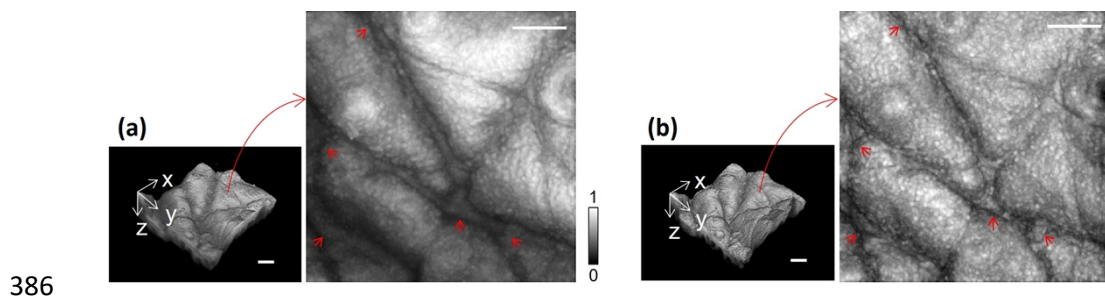


359

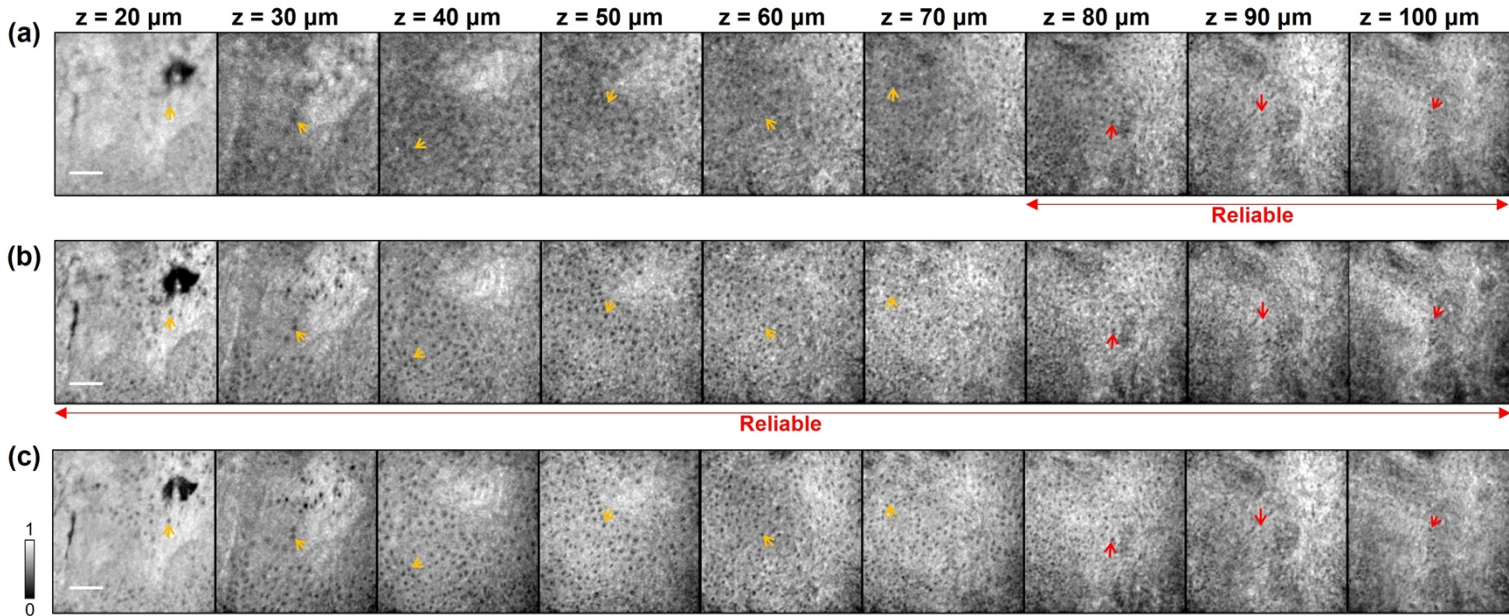
360 **Fig.S14** The XY images of 0.8µm microbeads captured by the OCT with the focused  
 361 Gaussian beam (20x water immersion objective), 80µm×1.5µm NB, and 300µm×3µm NB.  
 362 The XY images at the depths from -160µm to 160µm with 20µm interval are showed. The  
 363 Gaussian beam only produces high resolution image at  $z = 0$ , and the beads become barely  
 364 distinguishable beyond  $z < -40\mu\text{m}$  and  $z > 80\mu\text{m}$ . 80µm×1.5µm NB is able to clearly reveal  
 365 the individual beads in the depth range between -40µm and 40µm, and still can profile beads  
 366 at the depths of -60µm and 60µm. Outside the aforementioned depths, the XY-images are  
 367 completely out of focus and contain only noise. 300µm×3µm NB effectively detects single  
 368 beads for the whole depth range from -160µm to 160µm. Since NBs have sidelobes, the bead  
 369 profiles may have sidelobes at some specific depths. 80µm NB produces sidelobes in the XY-  
 370 images from  $z = -20\mu\text{m}$  to  $z = 20\mu\text{m}$ , and 300µm NB does from  $z = -40\mu\text{m}$  to  $z = 40\mu\text{m}$ .  
 371 The sidelobe ratios (SRs) are listed below the corresponding XY-images. The sidelobes have  
 372 limited effect on distinguishing closely adjacent beads, for example, the boundaries among  
 373 the adjacent beads marked by the red arrows are easily legible. GB, Gaussian beam; NB,  
 374 needle-shaped beam; WI, water immersion; SR, sidelobe ratio. Scale bar (in the last XY-  
 375 image), 10µm. The field-of-view is 50µm×50µm.

376 **3.3 Skin imaging**

377 Human tissue specimens that would otherwise have been discarded during surgical excision  
378 of skin growths were collected, placed in keratinocyte media, and stored at 4°C for an average  
379 of four hours before being transported to our lab. The specimens were stored in 10% formalin  
380 solution (VIP-Fixative, Scigen) at 4 °C in the laboratory refrigerator after being embedded in  
381 agar gel in Petri dishes. Informed consent was obtained from all subjects. All experimental  
382 protocols were approved by the Stanford Institutional Review Board (Protocol #48409), and  
383 all methods were carried out in accordance with relevant guidelines and regulations.  
384  
385



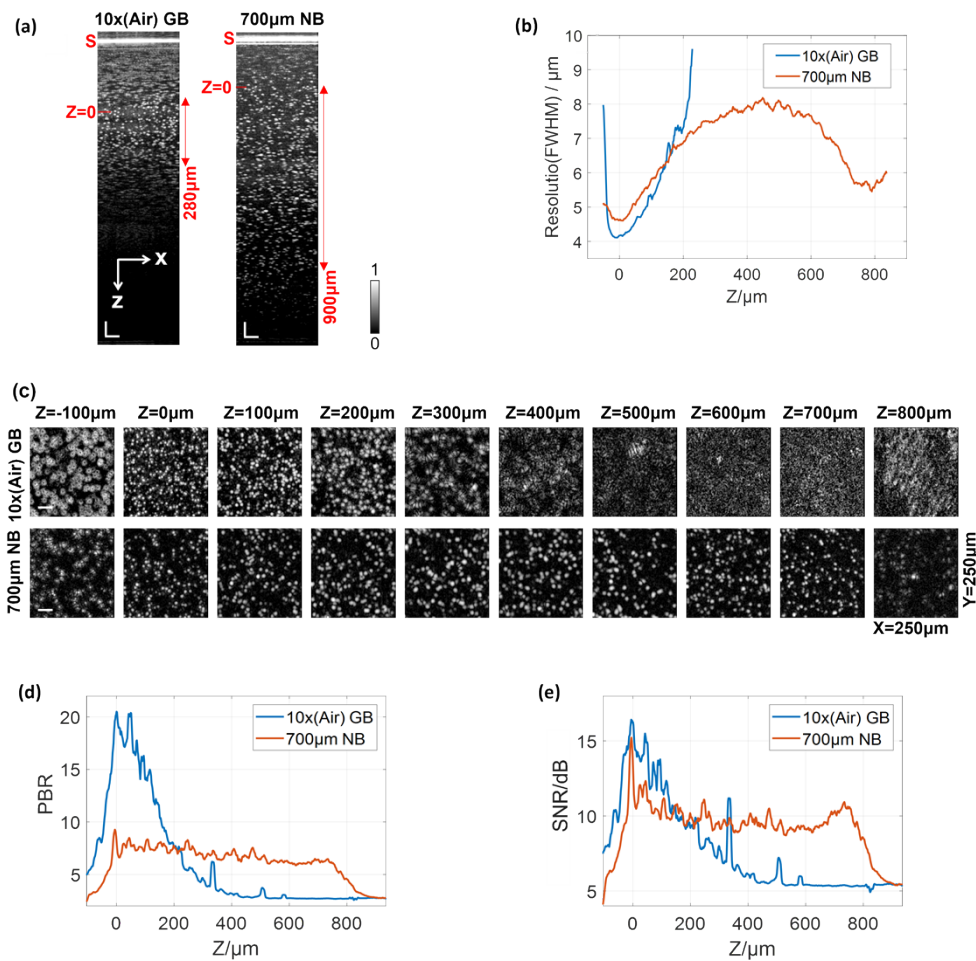
387 **Fig.S15** The surface projections of the 3D human skin images captured with Gaussian beam  
388 (20x water immersion lens) and 300µm×3µm NB. a, With Gaussian beam imaging, only the  
389 right upper region is in focus and the rest are blurry and dark. b, With 300µm×3µm NB, the  
390 details over the entire surface projection are revealed. Some comparisons are indicated by the  
391 red arrows. Scale bar, 200µm; XY-FOV, 1mm×1mm.



393 **Fig.S16** The XY images of human skin epidermis at the depths from  $z = 20\mu\text{m}$  to  $z =$   
 394  **$100\mu\text{m}$** . (a) Gaussian beam was focused (by 20x water immersion lens) at  $90\mu\text{m}$  depth. (b)  
 395  $80\mu\text{m} \times 1.5\mu\text{m}$  NB started at  $z = 20\mu\text{m}$  and ended at  $z = 100\mu\text{m}$ . (c) The all-in-focus images  
 396 were captured by axially focusing Gaussian beam at different depths. The XY-images of  
 397  $80\mu\text{m} \times 1.5\mu\text{m}$  NB are coincident with the all-in-focus images from  $z = 20\mu\text{m}$  to  $z = 100\mu\text{m}$   
 398 (e.g., both the cells marked by the red and yellow arrows are consistent), while the reliable  
 399 range for Gaussian beam is from  $z = 80\mu\text{m}$  to  $z = 100\mu\text{m}$  (e.g., only the cells marked by the  
 400 red arrows are consistent, but the cells marked by the yellows are not). Scale bar,  $100\mu\text{m}$ ;  
 401 XY-FOV,  $0.5\text{mm} \times 0.5\text{mm}$ . NB, needle-shaped beam; FOV, field-of-view.

402 3.4 Dynamic imaging of drosophila larva

403 In live imaging experiments, we used 3rd instar larvae of the standard laboratory wild-type  
 404 *Drosophila melanogaster* (Canton-S strain). Flies were raised on cornmeal agar media with a  
 405 12h light/dark cycle at 25°C and 50% relative humidity. All experimental protocols were  
 406 approved by the Stanford Institutional Review Board (Protocol #48409), and all methods  
 407 were carried out in accordance with relevant guidelines and regulations. **Visualization 1**  
 408 shows dynamic imaging of heartbeat, digestive system, and muscle motion.  
 409  
 410



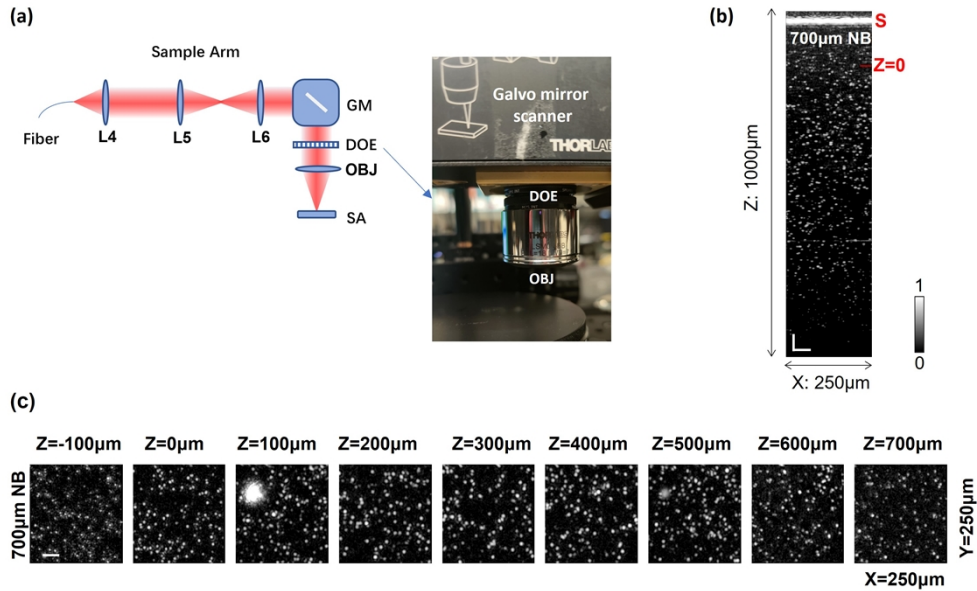
411

412 **Fig.S17** The images of 0.8µm microbeads captured by the OCT with Gaussian beam (10x dry  
 413 objective, LSM02-BB, Thorlabs) and 700µm×8µm NB. The beam profiles are given in  
 414 Supplementary Fig.9. 700µm×8µm NB here and 600µm×7.5µm NB in Supplementary Fig.9  
 415 were generated by the same diffractive optical element. The size changes because the  
 416 ultrasound gel used to contain the microbeads has a refractive index about 1.33, which is  
 417 larger than that of air (=1). (a) The B-scan images. The depth range where the beads are  
 418 clearly imaged is 280µm for Gaussian beam and 880µm for 700µm NB. S, the sample  
 419 surface. Scale bar, 50µm. (b) The resolution profiles. 700µm×8µm NB has a resolution  
 420 varying between 4.5µm (at the ends of the beam) and 8µm (in the middle). The resolution of  
 421 the Gaussian beam is down to 4µm but increases rapidly to 9.6µm at 230µm depth, and the

422 beads become indistinguishable in the depths deeper than  $230\mu\text{m}$  due to its resolution loss. (c)  
423 XY images. In Gaussian imaging, the beads located between  $z = 0$  and  $z = 200\mu\text{m}$  can  
424 produce complete circular profiles. For  $700\mu\text{m}$  NB, the range is from  $z = 0$  to  $z = 700\mu\text{m}$ .  
425 (d) The peak-to-background ratios (PBRs) along depth and (e) the signal-to-noise ratios (SNR) in  
426 the 3D bead images. In the depth range from  $200\mu\text{m}$  to  $800\mu\text{m}$ , the NB outperforms the  
427 focused Gaussian beam.  $\text{PBR} = (\text{peak intensity} - \text{average background intensity}) \div \text{average}$   
428  $\text{background intensity}$ ,  $\text{SNR} = (\text{peak intensity} - \text{average background intensity}) \div \text{standard}$   
429  $\text{deviation of background intensity}$ . Scale bar,  $50\mu\text{m}$ .  
430

431 **4. Discussion and conclusion**

432



433

434 **Fig.S18** The second configuration of OCT sample arm. (a) The sample arm in Supplementary  
 435 Fig.10 can use another configuration, where DOE is directly placed on the top of the objective  
 436 (OBJ) and just beneath the Galvo mirror (GM) scanner. Under this configuration,  
 437 700 μm × 8 μm NB was tested to image 0.8 μm microbeads. (b) The B-scan image of 0.8 μm  
 438 microbeads. S, the sample surface. Scale bar, 50 μm. (c) The XY images. Scale bar, 50 μm.  
 439 Referring to Supplementary Fig.13, the bead images taken with this configuration coincided  
 440 with those using the previous configuration.

441